CuSCN-Based Inverted Planar Perovskite Solar Cell with an Average PCE of 15.6%

ARTICLE *in* NANO LETTERS · MAY 2015

Impact Factor: 13.59 · DOI: 10.1021/acs.nanolett.5b00116 · Source: PubMed

8 AUTHORS, INCLUDING:

Senyun Ye
Peking University
8 PUBLICATIONS **35** CITATIONS
SEE PROFILE

Yunlong Li
Peking University
10 PUBLICATIONS **44** CITATIONS
SEE PROFILE

Weibo Yan
Peking University
23 PUBLICATIONS **134** CITATIONS
SEE PROFILE

Zuqiang Bian
Peking University
81 PUBLICATIONS **1,444** CITATIONS
SEE PROFILE

NANO LETTERS

Letter

pubs.acs.org/NanoLett

CuSCN-Based Inverted Planar Perovskite Solar Cell with an Average PCE of 15.6%

Senyun Ye,[†] Weihai Sun,[†] Yunlong Li,[†] Weibo Yan,[†] Haitao Peng,[‡] Zuqiang Bian,*[,†] Zhiwei Liu,*[,†] and Chunhui Huang[†]

[†]Beijng National Laboratory for Molecular Science, State Key Laboratory of Rare Earth Materials and Applications, College of Chemistry and Molecular Engineering, Peking University, Beijing 100871, People's Republic of China

[‡]Department of Energy and Resources Engineering, College of Engineering, Peking University, Beijing 100871, People's Republic of China

S *Supporting Information*

ABSTRACT: Although inorganic hole-transport materials usually possess high chemical stability, hole mobility, and low cost, the efficiency of most of inorganic hole conductor-based perovskite solar cells is still much lower than that of the traditional organic hole conductor-based cells. Here, we have successfully fabricated high quality $CH_3NH_3PbI_3$ films on top of a CuSCN layer by utilizing a one-step fast deposition-crystallization method, which have lower surface roughness and smaller interface contact resistance between the perovskite layer and the selective contacts in comparison with the films prepared by a conventional two-step sequential deposition process. The average efficiency of the CuSCN-based inverted planar $CH_3NH_3PbI_3$ solar cells has been improved to 15.6% with a highest PCE of 16.6%, which is comparable to that of the traditional organic hole conductor-based cells, and may promote wider application of the inexpensive inorganic materials in perovskite solar cells.

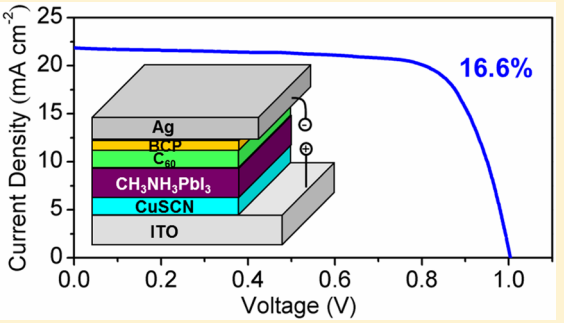

KEYWORDS: *Perovskite, solar cell, CuSCN, hole conductor*

Hybrid organic−inorganic perovskites currently exhibit rather strong competence among absorbers of thin-film photovoltaics, owing to their excellent light harvesting, high charge carrier mobility, and long electron- and hole-transport lengths.[1−3] Various photovoltaic architectures based on this remarkable material have been created and have achieved impressive power conversion efficiencies (PCEs). The conventional-architecture perovskite solar cells, which usually sandwich the perovskite layer between a mesoporous or compact metal-oxide photoanode and a hole-transport layer such as 2,2,7,7-tetrakis(*N*,*N*-di-*p*-methoxyphenylamine)-9,9-spirobifluo-rene (Spiro-OMeTAD), have reached a PCE over 15%.[4−7] Recently, poly(triarylamine) (PTAA) has been used as a novel organic hole-transport material in this type of perovskite solar cell with a PCE over 18%.[8] Meanwhile, the PCE of the inverted perovskite solar cells using poly(3,4-ethylenedioxythiophene):polystyrenesulfonate (PEDOT:PSS) as the hole conductor has also been over 15%.[9,10] However, the organic hole conductors are relatively costly, which may limit the future development and application of this type of solar cells. PEDOT:PSS is also not an ideal hole-transport material because of its inefficient electron-blocking capability and poor chemical stability stemming from its hygroscopic nature.[11−13]

In comparison with organic hole conductors, p-type inorganic materials usually possess high chemical stability, hole mobility, and low cost. There have been several reports about employing inorganic semiconductors as hole-transport materials in perovskite solar cells. Kamat et al.[14] first reported a PCE of 6.0% replacing spiro-OMeTAD with CuI, and then Nazeeruddin et al.[15] improved the PCE to 12.4% with CuSCN as a hole conductor in the conventional-architecture perovskite solar cells. Also, CuSCN and NiO have been explored in the inverse architecture perovskite solar cells with PCEs of 3.8%[16] and 9.1%,[17] respectively. Recently, Jen et al.[18] have employed a Cu-doped NiO as the hole-extraction layer and achieved an efficiency of 15.4%. However, the reported PCEs of most of the inorganic hole conductor-based perovskite solar cells[19−22] are still much lower than that of cells with organic hole conductors, which may attribute to the poor quality of perovskite films on top of the inorganic hole-conductor layers.

In this Letter, we choose an electrodeposited CuSCN film as the hole-transport layer due to its excellent transparency in the visible light spectrum range, high hole mobility, relatively good chemical stability, and simple preparation process.[23−26] High quality $CH_3NH_3PbI_3$ films on top of the CuSCN layer have been successfully fabricated by utilizing a one-step fast

Received: January 11, 2015
Revised: April 23, 2015

DOI: 10.1021/acs.nanolett.5b00116
Nano Lett. XXXX, XXX, XXX−XXX

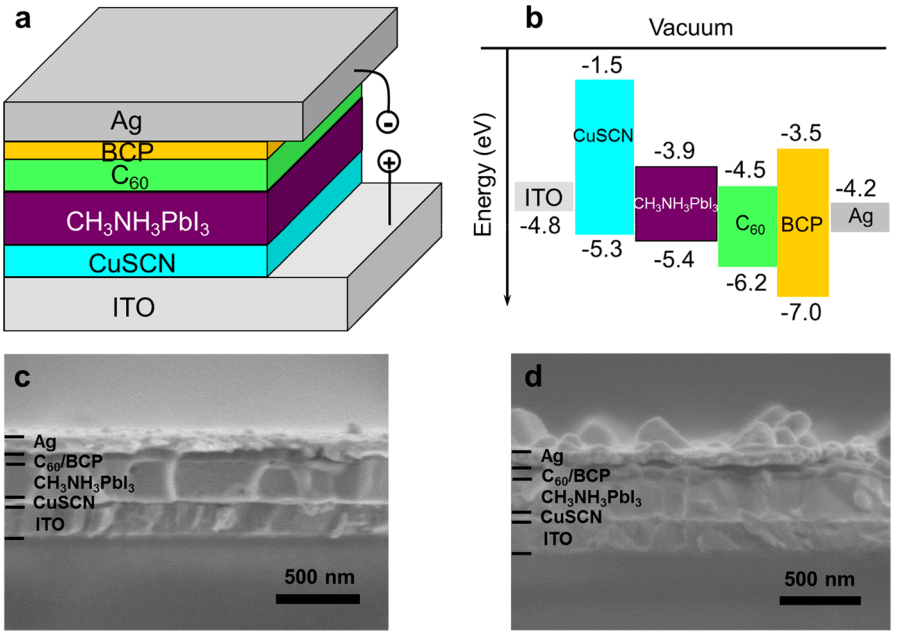

Figure 1. (a) Schematic illustration of the inverted CuSCN-based perovskite solar cell architecture. (b) Energy level diagram of each layer in the cell. SEM cross-sectional images of the cells with $CH_3NH_3PbI_3$ perovskites fabricated by the one-step fast deposition-crystallization method (c) and the conventional two-step sequential deposition process (d).

deposition-crystallization method (labeled as $CH_3NH_3PbI_3$ (one-step)). Compared with the perovskite films prepared by a conventional two-step sequential deposition process (labeled as $CH_3NH_3PbI_3$ (two-step)), the former possesses lower surface roughness and smaller interface contact resistance between the perovskite layer and the selective contacts. After optimization, a maximum PCE of 16.6% has been obtained with the $CH_3NH_3PbI_3$ (one-step), which is, as far as we know, the highest reported efficiency for perovskite solar cells using inorganic semiconductors as the hole-transport materials. Moreover, this is a comparable efficiency of perovskite solar cells based on inorganic hole conductors comparing with that of cells using organic hole conductors, which may improve the application prospect of inorganic hole conductors in the perovskite solar cells.

Optimized Device Structure. The inverted CuSCN-based $CH_3NH_3PbI_3$ solar cell configuration and energy levels of each layer in the cell are shown in Figure 1. The CuSCN film confirmed by the X-ray photoelectron spectroscopy (XPS) (Supporting Information, Figure S1) was electrodeposited on a cleaned indium tin oxide (ITO)-coated glass as a hole-transport layer before spin-coating the $CH_3NH_3PbI_3$ overlayer. The electrodeposition time was varied to obtain CuSCN films with different thickness. When the electrodeposition time increased to 50 s with other conditions consistent (see Methods), the ITO can be almost fully covered with the CuSCN film (optimized thickness: 57 ± 2 nm), which is expected to efficiently block contact between the ITO and the $CH_3NH_3PbI_3$ (Supporting Information, Figures S2 and S3). The light absorber, $CH_3NH_3PbI_3$, was then introduced using a one-step fast deposition-crystallization method with an optimized thickness of 214 ± 2 nm (Supporting Information, Figure S4). As a comparison, the $CH_3NH_3PbI_3$ film with almost the same thickness (215 ± 2 nm) was prepared by a conventional two-step sequential deposition process. After the same annealing treatment, 50 nm thick C_{60} layer, 8 nm thick bathocuproine (BCP) layer, and 100 nm thick silver layer were introduced as the electron collector, the hole blocker, and the cathode, respectively.

The XRD patterns of $CH_3NH_3PbI_3$ (one-step) and $CH_3NH_3PbI_3$ (two-step) films with almost the same thickness deposited on a CuSCN layer on the ITO-coated glass substrate are shown in Figure 2. The characteristic perovskite diffraction

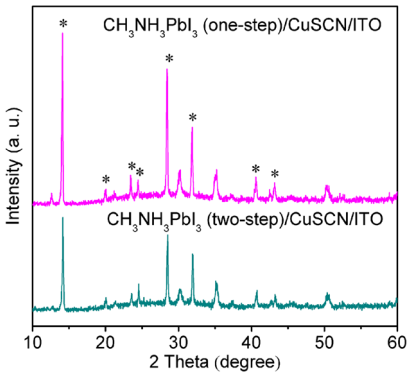

Figure 2. XRD patterns of $CH_3NH_3PbI_3$ (one-step)/CuSCN/ITO and $CH_3NH_3PbI_3$ (two-step)/CuSCN/ITO.

peaks marked with asterisks can be obviously observed in both $CH_3NH_3PbI_3$ films, and the peak at $2\theta \approx 12.6°$ attributing to the PbI_2 phase just displays a very weak intensity, indicating that the $CH_3NH_3PbI_3$ perovskites with high purity were successfully prepared by either a one-step fast deposition-crystallization method or a conventional two-step sequential deposition process.

Figure 3 illustrates the three-dimensional structures of the ITO-coated glass, the CuSCN film electrodeposited on an ITO/glass substrate, and the $CH_3NH_3PbI_3$ (one-step) and $CH_3NH_3PbI_3$ (two-step) layers deposited on respective CuSCN/ITO/glass substrates. The root-mean-square (RMS) roughness of the ITO-coated glass is 4.6 nm, while the RMS roughness sharply increases to 19.3 nm after being electro-

DOI: 10.1021/acs.nanolett.5b00116
Nano Lett. XXXX, XXX, XXX−XXX

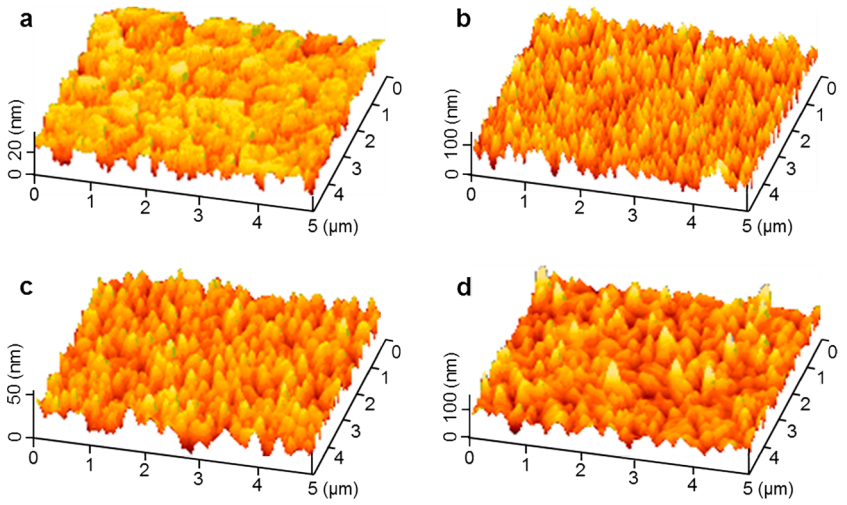

Figure 3. AFM images of ITO/glass (a), CuSCN/ITO/glass (b), $CH_3NH_3PbI_3$ (one-step)/CuSCN/ITO/glass (c), and $CH_3NH_3PbI_3$ (two-step)/CuSCN/ITO/glass (d). The RMS roughness values are 4.6, 19.3, 7.6, and 17.0 nm, respectively.

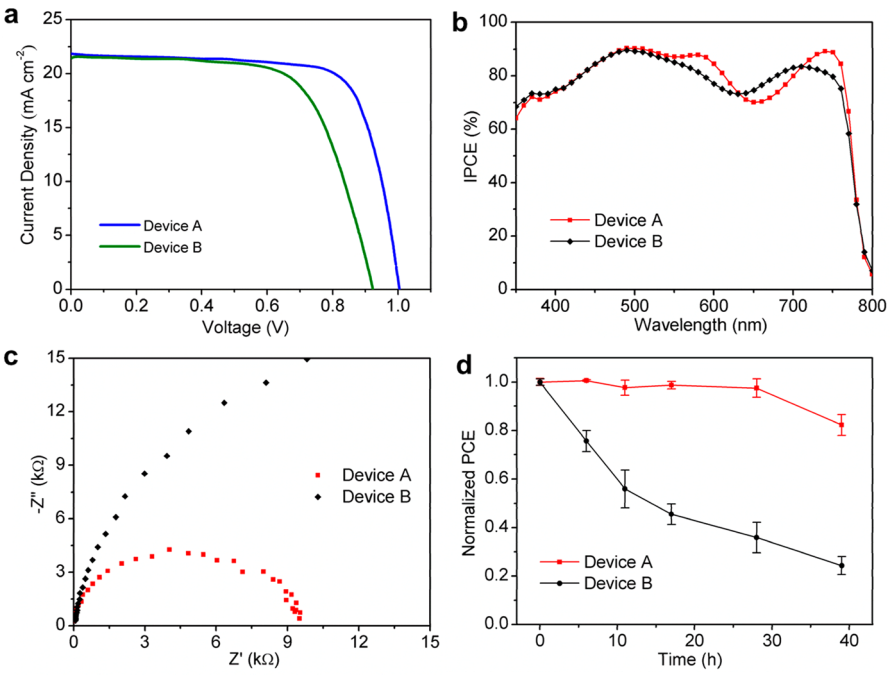

Figure 4. (a) Short circuit to forward bias current density−voltage characteristics of the champions of Device A (ITO/CuSCN/$CH_3NH_3PbI_3$ (one-step)/C_{60}/BCP/Ag) and Device B (ITO/CuSCN/$CH_3NH_3PbI_3$ (two-step)/C_{60}/BCP/Ag) measured under AM 1.5G 100 mW cm^{-2} simulated sun light at a scan rate of 0.5 V s^{-1}. (b) The corresponding IPCE spectra of Device A and Device B. (c) Nyquist plots of Device A and Device B under dark at the same applied voltage, 0.70 V. (d) Normalized PCE of unsealed Device A and Device B plotted as a function of storage time in ambient air in the dark (the measurements were the average of at least three devices).

deposited with a CuSCN film. The surface roughness of the subsequent $CH_3NH_3PbI_3$ (one-step) layer with a RMS roughness of 7.6 nm is much smaller than that of the $CH_3NH_3PbI_3$ (two-step) layer whose RMS roughness reaches as high as 17.0 nm. In addition, the maximum surface relief amplitude (SRA) of the $CH_3NH_3PbI_3$ (one-step) film is just 47.9 nm (Supporting Information, Figure S5a), which means 50 nm thick C_{60} layer can efficiently block contact between the $CH_3NH_3PbI_3$ and the silver cathode. However, the maximum SRA of the $CH_3NH_3PbI_3$ (two-step) film unexpectedly increases to 109.2 nm (Supporting Information, Figure S5b), indicating that some of the $CH_3NH_3PbI_3$ particles can poke through the subsequently deposited C_{60} and BCP to reach the silver cathode.

Photovoltaic Performance. Figure 4a shows typical curves of the short circuit to forward bias (SC-FB) current density−voltage (J−V) characteristics under AM 1.5G 100 mW cm^{-2} simulated sun light at a scan rate of 0.5 V s^{-1} for the respective champions of Device A (ITO/CuSCN/$CH_3NH_3PbI_3$ (one-step)/C_{60}/BCP/Ag) and Device B (ITO/CuSCN/$CH_3NH_3PbI_3$ (two-step)/C_{60}/BCP/Ag), which share almost the same configuration and preparation techniques except the method for fabricating $CH_3NH_3PbI_3$ films. The photovoltaic parameters of Device A and Device B are summarized in Table 1, and all the parameters were obtained from the SC-FB J−V

DOI: 10.1021/acs.nanolett.5b00116
Nano Lett. XXXX, XXX, XXX−XXX

Table 1. Photovoltaic Parameters of a Batch of Device A (ITO/CuSCN/$CH_3NH_3PbI_3$ (One-Step)/C_{60}/BCP/Ag) and Device B (ITO/CuSCN/$CH_3NH_3PbI_3$ (Two-Step)/C_{60}/BCP/Ag) Cells

cell architecture		V_{OC} (V)	*FF* (%)	J_{SC} (mA cm^{-2})	PCE (%)
Device A	champion	1.00	75.8	21.9	16.6
	mean ± SD[a]	0.97 ± 0.02	74.2 ± 1.4	21.7 ± 0.4	15.6 ± 0.6
Device B	champion	0.92	68.1	21.4	13.4
	mean ± SD[a]	0.92 ± 0.01	63.2 ± 4.4	18.9 ± 1.9	11.0 ± 1.5

[a]The mean values are calculated from a batch of 18 cells.

curves unless specified otherwise. Device A exhibits a PCE of 16.6% including an open-circuit voltage (V_{OC}) of 1.00 V, a fill factor (*FF*) of 75.8%, and a short circuit current density (J_{SC}) of 21.9 mA cm^{-2}, which slightly increases to 17.1% when using the opposite scan direction from forward bias to short circuit (FB-SC) (Supporting Information, Figure S6). As predicted, Device B shows a much lower PCE of 13.4%, and the efficiency also increases to 14.0% when using the FB-SC scan direction (Supporting Information, Figure S6). Although the PCE of both devices varies with the scan direction, known as an anomalous hysteresis effect present widespread in the *J*−*V* curves of perovskite solar cells,[27,28] the severity of the effect is not conspicuous in both devices. In comparison with Device A, the lower efficiency of Device B is mainly attributed to the relatively low V_{OC} (0.92 V) and *FF* (68.1%). The J_{SC} of Device B (21.4 mA cm^{-2}) is only slightly less than that of Device A, in agreement with the integrated J_{SC} (20.7 mA cm^{-2} of Device B versus 21.1 mA cm^{-2} of Device A) calculated from the incident photon to current conversion efficiency (IPCE) spectra (Figure 4b). The lower V_{OC} of Device B is probably due to the large surface relief amplitude of the $CH_3NH_3PbI_3$ (two-step) film on top of the rough CuSCN layer confirmed by the AFM study, which will lead to direct contact of the $CH_3NH_3PbI_3$ with the silver cathode and cause some current leakage paths. This is consistent with a smaller shunt resistance of Device B (867 Ω cm^2) than that of Device A (1210 Ω cm^2), calculated from the fitting of the *J*−*V* curves, which will simultaneously result in a poorer *FF*. In addition, a higher series resistance of Device B is also a significant reason for the poorer *FF* (8.7 Ω cm^2 of Device B versus 4.6 Ω cm^2 of Device A calculated from the fitting of the *J*−*V* curves), which is further confirmed by the electrochemical impedance spectroscopy (EIS). As shown in Figure 4c, the arcs at high-intermediate frequency are mainly attributed to the charge-transport resistance at the interface of the selective contacts with the perovskite layer.[29−32] Consequently, the charge-transport resistance at the $CH_3NH_3PbI_3$ (one-step)/selective contacts interface is lower than that at the $CH_3NH_3PbI_3$ (two-step)/selective contacts interface, leading to a lower series resistance of Device A than Device B. This result may be attributed to the difference between the $CH_3NH_3PbI_3$ (one-step) film and the $CH_3NH_3PbI_3$ (two-step) film. As shown in Figure S7, the $CH_3NH_3PbI_3$ (two-step) film exhibits more and larger cracks than that of $CH_3NH_3PbI_3$ (one-step) film, which may reduce the carrier transport efficiency. This indicates that the interface contact resistance between the perovskite layer and the selective contacts can be effectively decreased by preparing the perovskite layer with the one-step fast deposition-crystallization method.

In order to ensure the credibility of our results, a batch of Device A and Device B, respectively, containing 18 cells, were fabricated and tested under the same conditions. As shown in Table 1, the differences in V_{OC}, *FF*, and PCE between Device A and Device B are conspicuously beyond their associated standard deviations, suggesting that the differences are indeed attributed to the diversity between the two perovskite film preparation processes, rather than the batch-to-batch variation. Furthermore, the reproducibility of Device A is much better than that of Device B, indicating the high uniformity of perovskite layer on top of the rough CuSCN film fabricated by the one-step fast deposition-crystallization method. The stability of Device A and Device B was also investigated. Figure 4d shows the loss in PCE over time with the unsealed devices storage in the same ambient air in the dark. Device B degrades quickly as exposed to air, while the performance of Device A keeps almost invariable in the first 28 h. The worse stability of Device B may result from the inefficient coverage of the $CH_3NH_3PbI_3$ (two-step) layer with large surface relief amplitude by the subsequent overlayers, which makes air easy to reach the perovskite layer, leading to decomposition of the perovskite. Moreover, the stabilized power output under working conditions of Device A has also been confirmed (Supporting Information, Figure S8b).

In summary, we have demonstrated the feasibility obtaining high-quality $CH_3NH_3PbI_3$ perovskite films on top of a rough CuSCN layer by a one-step fast deposition-crystallization method, and first improved the efficiency of inorganic hole conductor-based perovskite solar cells over 16%. In comparison with the $CH_3NH_3PbI_3$ film on top of a rough CuSCN layer fabricated by a conventional two-step sequential deposition process, the $CH_3NH_3PbI_3$ (one-step) film possesses lower surface roughness and smaller interface contact resistance between the perovskite layer and the selective contacts, which mostly leads to higher V_{OC}, *FF*, and PCE. Furthermore, the CuSCN-based $CH_3NH_3PbI_3$ (one-step) perovskite solar cells have higher reproducibility and stability.

Methods. *Device Fabrication.* The ITO-coated glass substrates were first ultrasonically cleaned with detergent, acetone, ethyl alcohol, and deionized water in sequence. The CuSCN layers were then potentiostatically electrodeposited from an aqueous solution containing 12 mM copper sulfate ($CuSO_4$), 12 mM ethylenediaminetetraacetic acid (EDTA) and 12 mM potassium thiocyanate (KSCN) at a fixed potential of −0.3 V versus Ag/AgCl (3 M KCl) electrode.[33,34] In order to fabricate CuSCN layers with different thickness, the electrodeposition time was varied from 7 to 100 s. After drying with nitrogen, the CuSCN/ITO/glass substrates were deposited with a layer of $CH_3NH_3PbI_3$ by either a one-step fast deposition-crystallization method[35] or a conventional two-step sequential deposition process[4] in a N_2-purged glovebox (<1.0 ppm of O_2 and H_2O). Finally, 50 nm of C_{60}, 8 nm of BCP, and 100 nm of Ag were sequentially thermally evaporated under a high vacuum through a shadow mask with an active area of 0.10 cm^2.

$CH_3NH_3PbI_3$ (One-Step) Film Preparation. The $CH_3NH_3PbI_3$ solution in DMF with various concentration

DOI: 10.1021/acs.nanolett.5b00116
Nano Lett. XXXX, XXX, XXX−XXX

(35, 43, 45, and 47 wt %) was spin-coated at 5000 rpm for 30 s on the CuSCN/ITO/glass substrate to obtain the $CH_3NH_3PbI_3$ (one-step) layer with different thickness (149 ± 2, 214 ± 2, 257 ± 2, and 284 ± 2 nm). After about 4.5 s of the spin-coating, 200 μL of chlorobenzene was quickly added to induce the fast crystallization. Subsequently, the $CH_3NH_3PbI_3$ (one-step) perovskite was annealed at 100 °C for 10 min.

$CH_3NH_3PbI_3$ (Two-Step) Film Preparation. A DMF solution of PbI_2 (462 mg mL^{-1}, 70 °C) was first spin-coated at 5000 rpm for 60 s on top of the CuSCN layer. After drying at room temperature (RT) for about 30 min, the PbI_2/CuSCN/ITO glass substrate was immersed in a CH_3NH_3I isopropanol solution (10 mg mL^{-1}, RT) for about 10 min to form the $CH_3NH_3PbI_3$ (two-step) perovskite. Then, the substrate was dried with nitrogen and annealed at 100 °C for 10 min.

Measurement and Characterization. The *J*−*V* curves of photovoltaic devices were measured under AM 1.5G 100 mW cm^{-2} simulated sun light by using the Keithley 4200 System in cooperation with the Oriel 300 W solar simulator (Thermo Oriel 91160−1000). The IPCE spectra were recorded on a Keithley 2400 source meter working with a 1/4 m monochromator (Spectral Product DK240) under irradiation of a 150 W tungsten lamp. The thickness of CuSCN and $CH_3NH_3PbI_3$ perovskite films was determined by a KLA-Tencor α-Step Surface Profiler. The AFM and SEM images were obtained by utilizing SPA400 SPM (SeikoInstrument, Inc.) and Hitachi S-4800, respectively. The XRD patterns were recorded on a D/MAX-2000 X-ray diffractometer with monochromated Cu Kα irradiation (λ = 1.5418 Å). The electrodeposition of the CuSCN layer and the EIS measurements were performed on a CHI660 electrochemical workstation (CH Instrument, Inc.).

■ ASSOCIATED CONTENT

Supporting Information

Additional data including the XPS of CuSCN layer, the optimization of Device A with various $CH_3NH_3PbI_3$ film thickness and CuSCN layer thickness, the SEM images of CuSCN layer with different electrodeposition time, the planar AFM images of $CH_3NH_3PbI_3$ (one-step) and $CH_3NH_3PbI_3$ (two-step) films deposited on CuSCN/ITO/glass substrates, the *J*−*V* curves of champions of Device A and Device B with different scan direction, the *J*−*V* curves of Device A with different scan rate and the steady-state efficiency for Device A. The Supporting Information is available free of charge on the ACS Publications website at DOI: 10.1021/acs.nanolett.5b00116.

■ AUTHOR INFORMATION

Corresponding Authors

*E-mail: bianzq@pku.edu.cn.
*E-mail: zwliu@pku.edu.cn.

Notes

The authors declare no competing financial interest.

■ ACKNOWLEDGMENTS

This work was supported by the National Basic Research Program (2011CB933303) and the National Natural Science Foundation of China (NSFC) (21321001 and 21371012).

■ REFERENCES

(1) Cheng, Z. Y.; Lin, J. *CrystEngComm* **2010**, *12*, 2646−2662.
(2) Stranks, S. D.; Eperon, G. E.; Grancini, G.; Menelaou, C.; Alcocer, M. J. P.; Leijtens, T.; Herz, L. M.; Petrozza, A.; Snaith, H. J. *Science* **2013**, *342*, 341−344.
(3) Xing, G. C.; Mathews, N.; Sun, S. Y.; Lim, S. S.; Lam, Y. M.; Grätzel, M.; Mhaisalkar, S.; Sum, T. C. *Science* **2013**, *342*, 344−347.
(4) Burschka, J.; Pellet, N.; Moon, S. J.; Humphry-Baker, R.; Gao, P.; Nazeeruddin, M. K.; Grätzel, M. *Nature* **2013**, *499*, 316−319.
(5) Liu, D. Y.; Kelly, T. L. *Nat. Photonics* **2014**, *8*, 133−138.
(6) Liu, M. Z.; Johnston, M. B.; Snaith, H. J. *Nature* **2013**, *501*, 395−398.
(7) Zhou, H. P.; Chen, Q.; Li, G.; Luo, S.; Song, T. B.; Duan, H. S.; Hong, Z. R.; You, J. B.; Liu, Y. S.; Yang, Y. *Science* **2014**, *345*, 542−546.
(8) Jeon, N. J.; Noh, J. H.; Yang, W. S.; Kim, Y. C.; Ryu, S.; Seo, J.; Seok, S., II. *Nature* **2015**, *517*, 476−480.
(9) Chiang, C. H.; Tseng, Z. L.; Wu, C. G. *J. Mater. Chem. A* **2014**, *2*, 15897−15903.
(10) Xiao, Z. G.; Bi, C.; Shao, Y. C.; Dong, Q. F.; Wang, Q.; Yuan, Y. B.; Wang, C. G.; Gao, Y. L.; Huang, J. S. *Energy Environ. Sci.* **2014**, *7*, 2619−2623.
(11) Irwin, M. D.; Buchholz, B.; Hains, A. W.; Chang, R. P. H.; Marks, T. J. *Proc. Natl. Acad. Sci. U.S.A.* **2008**, *105*, 2783−2787.
(12) Jorgensen, M.; Norrman, K.; Krebs, F. C. *Sol. Energy Mater. Sol. Cells* **2008**, *92*, 686−714.
(13) Norrman, K.; Madsen, M. V.; Gevorgyan, S. A.; Krebs, F. C. *J. Am. Chem. Soc.* **2010**, *132*, 16883−16892.
(14) Christians, J. A.; Fung, R. C. M.; Kamat, P. V. *J. Am. Chem. Soc.* **2014**, *136*, 758−764.
(15) Qin, P.; Tanaka, S.; Ito, S.; Tetreault, N.; Manabe, K.; Nishino, H.; Nazeeruddin, M. K.; Grätzel, M. *Nat. Commun.* **2014**, *5*, 3834−3840.
(16) Subbiah, A. S.; Halder, A.; Ghosh, S.; Mahuli, N.; Hodes, G.; Sarkar, S. K. *J. Phys. Chem. Lett.* **2014**, *5*, 1748−1753.
(17) Zhu, Z. L.; Bai, Y.; Zhang, T.; Liu, Z. K.; Long, X.; Wei, Z. H.; Wang, Z. L.; Zhang, L. X.; Wang, J. N.; Yan, F.; Yang, S. H. *Angew. Chem., Int. Ed.* **2014**, *53*, 12571−12575.
(18) Kim, J. H.; Liang, P. W.; Williams, S. T.; Cho, N.; Chueh, C. C.; Glaz, M. S.; Ginger, D. S.; Jen, A. K.-Y. *Adv. Mater.* **2015**, *27*, 695−701.
(19) Zhao, Y. X.; Nardes, A. M.; Zhu, K. *Appl. Phys. Lett.* **2014**, *104*, 213906.
(20) Wang, K. C.; Shen, P. S.; Li, M. H.; Chen, S.; Lin, M. W.; Chen, P.; Guo, T. F. *ACS Appl. Mater. Interfaces* **2014**, *6*, 11851−11858.
(21) Wang, K. C.; Jeng, J. Y.; Shen, P. S.; Chang, Y. C.; Diau, E. W. G.; Tsai, C. H.; Chao, T. Y.; Hsu, H. C.; Lin, P. Y.; Chen, P.; Guo, T. F.; Wen, T. C. *Sci. Rep.* **2014**, *4*, 1−8.
(22) Chavhan, S.; Miguel, O.; Grande, H. J.; Gonzalez-Pedro, V.; Sanchez, R. S.; Barea, E. M.; Mora-Sero, I.; Tena-Zaera, R. *J. Mater. Chem. A* **2014**, *2*, 12754−12760.
(23) Chappaz-Gillot, C.; Berson, S.; Salazar, R.; Lechene, B.; Aldakov, D.; Delaye, V.; Guillerez, S.; Ivanova, V. *Sol. Energy Mater. Sol. Cells* **2014**, *120*, 163−167.
(24) Li, B.; Wang, L. D.; Kang, B. N.; Wang, P.; Qiu, Y. *Sol. Energy Mater. Sol. Cells* **2006**, *90*, 549−573.
(25) Pattanasattayavong, P.; Ndjawa, G. O. N.; Zhao, K.; Chou, K. W.; Yaacobi-Gross, N.; O'Regan, B. C.; Amassian, A.; Anthopoulos, T. D. *Chem. Commun.* **2013**, *49*, 4154−4156.
(26) Pattanasattayavong, P.; Yaacobi-Gross, N.; Zhao, K.; Ndjawa, G. O. N.; Li, J. H.; Yan, F.; O'Regan, B. C.; Amassian, A.; Anthopoulos, T. D. *Adv. Mater.* **2013**, *25*, 1504−1509.
(27) Snaith, H. J.; Abate, A.; Ball, J. M.; Eperon, G. E.; Leijtens, T.; Noel, N. K.; Stranks, S. D.; Wang, J. T. W.; Wojciechowski, K.; Zhang, W. *J. Phys. Chem. Lett.* **2014**, *5*, 1511−1515.
(28) Unger, E. L.; Hoke, E. T.; Bailie, C. D.; Nguyen, W. H.; Bowring, A. R.; Heumüller, T.; Christoforo, M. G.; McGehee, M. D. *Energy Environ. Sci.* **2014**, *7*, 3690−3698.
(29) Dualeh, A.; Moehl, T.; Tetreault, N.; Teuscher, J.; Gao, P.; Nazeeruddin, M. K.; Grätzel, M. *ACS Nano* **2014**, *8*, 362−373.

DOI: 10.1021/acs.nanolett.5b00116
Nano Lett. XXXX, XXX, XXX−XXX

(30) Zheng, L. L.; Chung, Y. H.; Ma, Y. Z.; Zhang, L. P.; Xiao, L. X.; Chen, Z. J.; Wang, S. F.; Qu, B.; Gong, Q. H. *Chem. Commun.* **2014**, *50*, 11196−11199.
(31) Juarez-Perez, E. J.; Wussler, M.; Fabregat-Santiago, F.; Lakus-Wollny, K.; Mankel, E.; Mayer, T.; Jaegermann, W.; Mora-Sero, I. *J. Phys. Chem. Lett.* **2014**, *5*, 680−685.
(32) Kim, H. S.; Mora-Sero, I.; Gonzalez-Pedro, V.; Fabregat-Santiago, F.; Juarez-Perez, E. J.; Park, N. G.; Bisquert, J. *Nat. Commun.* **2013**, *4*, 2242−2248.
(33) Chappaz-Gillot, C.; Salazar, R.; Berson, S.; Ivanova, V. *Electrochim. Acta* **2013**, *110*, 375−381.
(34) Chappaz-Gillot, C.; Salazar, R.; Berson, S.; Ivanova, V. *Electrochem. Commun.* **2012**, *24*, 1−4.
(35) Xiao, M. D.; Huang, F. Z.; Huang, W. C.; Dkhissi, Y.; Zhu, Y.; Etheridge, J.; Gray-Weale, A.; Bach, U.; Cheng, Y. B.; Spiccia, L. *Angew. Chem., Int. Ed.* **2014**, *53*, 9898−9903.

DOI: 10.1021/acs.nanolett.5b00116
Nano Lett. XXXX, XXX, XXX−XXX